OAK RIDGE
NATIONAL LABORATORY
MANAGED BY UT-BATTELLE
FOR THE DEPARTMENT OF ENERGY

ORNL/TM-2014/241

Comprehensive and Comparative Analysis of Atom Probe, Small-Angle Neutron Scattering, and Other Microstructural Experiments on Available High Fluence Reactor Pressure Vessel Steels

June 2014

Prepared by

M. A. Sokolov, R. K. Nanstad, M. K. Miller, and K. C. Littrell,
Oak Ridge National Laboratory, Oak Ridge, TN
G. R. Odette and P. Wells,
University of California – Santa Barbara, CA
D. J. Sprouster and L. E. Ecker,
Brookhaven National Laboratory, Upton, NY

UT-BATTELLE
ORNL-27 (4-00)

This page intentionally left blank

ORNL/TM-2014/241

Light Water Reactor Sustainability

COMPREHENSIVE AND COMPARATIVE ANALYSIS OF ATOM PROBE, SMALL-ANGLE NEUTRON SCATTERING, AND OTHER MICROSTRUCTURAL EXPERIMENTS ON AVAILABLE HIGH FLUENCE REACTOR PRESSURE VESSEL STEELS

M. A. Sokolov, R. K. Nanstad, M. K. Miller, and K. C. Littrell
Oak Ridge National Laboratory, Oak Ridge, TN
G. R. Odette and P. Wells,
University of California – Santa Barbara, CA
D. J. Sprouster and L. E. Ecker,
Brookhaven National Laboratory, Upton, NY

Date Published: June 2014

Prepared under the direction of the
U.S. Department of Energy Office of
Nuclear Energy
Light Water Reactor Sustainability
Materials Aging and Degradation Pathway

Prepared by
OAK RIDGE NATIONAL LABORATORY
Oak Ridge, Tennessee 37831-6283
managed by
UT-BATTELLE, LLC
for the
U.S. DEPARTMENT OF ENERGY
under contract DE-AC05-00OR22725

This page intentionally left blank

CONTENTS

Page

This page intentionally left blank

LIST OF FIGURES

This page intentionally left blank

LIST OF TABLES

This page intentionally left blank

ACKNOWLEGEMENTS

This research was sponsored by the U.S. Department of Energy, Office of Nuclear Energy, for the Light Water Reactor Sustainability Research and Development effort. The authors extend their appreciation to Dr. Jeremy Busby for programmatic support and to Dr. Yukinori Yamamoto for technical review. Atom probe tomography research was sponsored through a user project supported by ORNL's Center for Nanophase Materials Sciences (CNMS), which is sponsored by the Scientific User Facilities Division, Office of Basic Energy Sciences, U.S. Department of Energy. The small angle neutron scattering research at ORNL's High Flux Isotope Reactor was sponsored by the Scientific User Facilities Division, Office of Basic Energy Sciences, U.S. Department of Energy. For the NIST Center for Neutron Research small angle neutron scattering results, the authors acknowledge the support of the National Institute of Standards and Technology, U.S. Department of Commerce, in providing the neutron research facilities used in this work. Funding for part of this research was provided by the DOE Office of Nuclear Energy's Nuclear Energy University Programs.

This page intentionally left blank

1. INTRODUCTION

The reactor pressure vessel (RPV) in a light-water reactor (LWR) represents the first line of defense against a release of radiation in case of an accident. Thus, regulations that govern the operation of commercial nuclear power plants require conservative margins of fracture toughness, both during normal operation and under accident scenarios. In the unirradiated condition, the RPV has sufficient fracture toughness such that failure is implausible under any postulated condition, including pressurized thermal shock (PTS) in pressurized water reactors (PWR). In the irradiated condition, however, the fracture toughness of the RPV may be severely degraded, with the degree of toughness loss dependent on the radiation sensitivity of the materials. As stated in previous progress reports, the available embrittlement predictive models, e.g. [1], and our present understanding of radiation damage are not fully quantitative, and do not treat all potentially significant variables and issues, particularly considering extension of operation to 80y.

The major issues regarding irradiation effects are discussed in [2, 3] and have also been discussed in previous progress and milestone reports. As noted previously, of the many significant issues discussed, the issue considered to have the most impact on the current regulatory process is that associated with effects of neutron irradiation on RPV steels at high fluence, for long irradiation times, and as affected by neutron flux. It is clear that embrittlement of RPV steels is a critical issue that may limit LWR plant life extension. The primary objective of the LWRSP RPV task is to develop robust predictions of transition temperature shifts (TTS) at high fluence (φt) to at least 1020 n/cm2 (>1 MeV) pertinent to plant operation of some pressurized water reactors (PWR) for 80 full power years. Correlations between the high flux test reactor results and low flux surveillance specimens must be established for proper RPV embrittlement predictions of the current nuclear power fleet. Additionally, a complete understanding of defect evolution for high nickel RPV steels is needed to characterize the embrittlement potential of Mn-Ni-enriched precipitates (MNPs), particularly for the high fluence regime. While understanding of copper-enriched precipitates (CRPs) have been fully developed, the recent discovery and experimental verification [4] of 'late blooming' MNPs with little to no copper for nucleation has stimulated research efforts to understand the evolution of these phases. New and existing databases will be combined to support developing physically based models of TTS for high fluence-low flux (φ < 10 11n/cm2-s) conditions, beyond the existing surveillance database, to neutron fluences of at least 1×1020 n/cm2 (>1 MeV). All references to neutron flux and fluence in this report are for fast neutrons (>1 MeV). Moreover, a large number of various RPV materials has been irradiated in ATR-2 experiment and will be jointly studied by University of California, Santa Barbara (UCSB) and ORNL to address the majority of microstructural characteristics discussed above, see Ref. [5] and [6] for details. UCSB has performed a large number of SANS experiments in the past at the National Institute of Standards and Technology (NIST) Center for Neutron Research (NCNR). These data are taken from RPV steels irradiated in a wide range of flux-fluence space and will be very useful in comparing to the upcoming UCSB ATR-2 irradiation characterization. Since most of the SANS experiments with ATR-2 materials will be performed at ORNL High Flux Isotope Reactor (HFIR), it important to confirm that HFIR and NCNR give the same results within reasonable error. To confirm the repeatability of measurements at both facilities, SANS experiments were performed on RPV materials irradiated in the UCSB ATR-1 irradiation as well as surveillance material obtained by ORNL at both NCNR and HFIR.

The RPV task of the LWRS Program is working with various organizations to obtain archival surveillance materials from commercial nuclear power plants to allow for comparisons of the irradiation-induced microstructural features from reactor surveillance materials with those from similar

materials irradiated under high flux conditions in test reactors. This report provides the status for the Level 2 Milestone (M2LW-140R0402013), "Complete report on comprehensive and comparative analysis of Atom Probe and Small-angle Neutron Scattering Experiments on available high fluence reactor pressure vessel steel specimens." This milestone is associated with microstructural characterization of materials from commercial power reactors, R. E. Ginna and Ringhals, as well as examinations of materials irradiated in the BR-2 test reactor.

2. RESULTS OF MICROSTRUCTURAL EXAMINATIONS

2.1 BACKGROUND AND DESCRIPTION OF MATERIALS

In [7], materials for five different projects were described and discussed; (1) Materials for the ATR-2 experiment, (2) Materials from the Zion reactor, (3) Materials from the Ringhals reactors, (4) Materials from the R. E. Ginna reactor, and (5) Materials from the Palisades reactor. The reader is referred to [4-7] for more detailed discussion of those projects.

A detailed description of the materials from the Ringhals Reactors was presented in [8,9] and will only be summarized in this report. Dr. Pal Efsing of Vattenfall AB in Sweden has provided small samples of surveillance materials removed from tested Charpy impact specimens. All the surveillance specimens are from low-copper high-nickel weld metals in Ringhals Units 3 and 4, both pressurized water reactors. These specimens have been used to prepare samples for atom probe tomography and small-angle neutron scattering to characterize the microstructure relative to irradiation-induced precipitates and other defects, and the results are discussed in Section 2.2.

Materials from the R.E. Ginna reactor were described in [10], and additional updated information is discussed in this report in Section 2.3.

Background on Ringhals RPV Materials

The primary interest in these weld metals is because they are very high in nickel content, with 1.58 and 1.66 wt% for Unit 3 and Unit 4, respectively, as shown in Table 2.1. For reference, the highest nickel content in the U.S. Nuclear Regulatory Commission Regulatory Guide 1.99, Rev. 2 is 1.20 wt% [11]. As stated by Efsing, et. al. [12], the nickel content in Unit 4 is the highest reported nickel content for any Westinghouse PWR. This high nickel content is, as mentioned previously, the primary reason for interest in examination of the irradiated microstructure of the Ringhals welds. As expected for such high nickel welds, both weld metals have exhibited very high irradiation-induced Charpy 41-J transition temperature shifts (ΔTT_{41}) in surveillance testing [12]:

1. For Unit R3, ΔTT_{41} of 192°C (345°F) at 5.0×10^{19} n/cm^2 (>1 MeV)
2. For Unit R4, ΔTT_{41} of 162°C (292°F) at 6.0×10^{19} n/cm^2 (>1 MeV)

Thus, the radiation sensitivity of both weld metals is extremely high in spite of their low copper contents. Vattenfall AB in Sweden provided ORNL with small samples of surveillance materials removed from tested Charpy impact specimens from Ringhals Units R3 and R4, with neutron fluences from 3.3 to 6.4×10^{19} n/cm^2 and average neutron flux of about 1.4×10^{11} n/cm^2/s. As shown in Table 2.1, the nickel contents are about 1.6 wt% with copper contents of 0.08 wt% or less. The samples provided by Vattenfall AB are slices from Charpy impact specimens and are about 10×10×0.4 mm thick. As stated earlier, these materials are of high interest to the LWRS Program because they have low copper and high

nickel contents, have been irradiated to relatively high neutron fluences, and exhibit very significant radiation sensitivity as indicated by the very high Charpy ΔTT_{41} values.

Table 1 Compositions of the two Ringhals RPV materials used in this study. Fe is the balance.

Material	C	Si	Mn	P	S	Cr	Mo	Ni	Cu	Al	Co	V
R3-(E) wt%	0.052	0.21	1.46	0.009	0.006	0.07	0.54	1.58	0.08	0.027	0.015	0.002
R4-(N) wt%	0.068	0.14	1.35	0.015	0.004	0.04	0.50	1.66	0.05	0.024	0.010	0

Background on Ginna RPV Materials

The following information regarding the materials and surveillance test results has been taken from [13]. The weld material from the Ginna surveillance program comes from the circumferential weld joining intermediate shell forging (Heat 125S255) and lower shell forging (Heat 125P666). The weld is heat number 61782 (this is the weld wire heat no.) and, with the flux lot 8350, is a Linde 80 weld designated SA-847. The heat-affected-zone (HAZ) specimens come from the HAZ between the circumferential weld and lower shell forging (Heat 125P666). The weld metal chemical composition includes 0.23% Cu, 0.53% Ni, and 1.31% Mn, while the forging chemical composition includes 0.05% Cu, 0.69% Ni, and 0.67% Mn (all wt%). Five capsules have been removed and tested over the course of reactor operation at neutron fluences ranging from 0.58×10^{19} to 5.8×10^{19} n/cm^2. The specimens provided to ORNL were irradiated to 1.69, 3.64, and 5.80×10^{19} n/cm^2; for those three fluences, ΔTT_{41} values for the weld specimens were 82 to 121°C and those for the forging were 19 to 51°C. The reactor coolant temperature (assumed to be the irradiation temperature for the surveillance specimens) is given as 285 to 289°C. The latest removal, Capsule N, was performed after 30.5 effective full power years of plant operation. All received specimens are tested Charpy impact specimens from surveillance capsules, with average neutron flux of 7×10^{10} n/cm^2/s. As expected based on the higher copper content of the weld relative to the forging, the weld exhibits significantly greater irradiation-induced shifts vs neutron fluence.

Background on Materials Irradiated in BR-2 Test Reactor

The NRC-funded Heavy-Section Steel Irradiation (HSSI) Program had previously irradiated various RPV steels at fluxes of about 4 to 8×10^{11} n/cm^{2}s to fluences from 0.5 to 3.4×10^{19} n/cm^2 and at 288°C. The HSSI Program provided tensile and 5x10-mm three-point bend specimens (0.2TSEB) of five materials to SCK-CEN for irradiation in the in-pile section #3 (IPS-3) of the Belgian Reactor BR2 at fluxes $>10^{13}$ n/cm^2/s to the same fluences as previous low flux irradiations to enable direct evaluations of flux effects. The BR2 irradiations were conducted at fluxes of about 2 and $4x10^{13}$ n/cm^2/s with irradiation temperatures from 295 to 300°C (water temperature). The reader is referred to [14] for more detailed description of the irradiation experiment in BR2. Unfortunately, fluences ranged from about 6-10x10^{19} n/cm^2 (0.10-0.16 dpa) more than double the desired fluences, making direct comparisons of irradiation-induced fracture toughness shifts and evaluations of flux effects confounded by significantly different fluences. Table 2.2 provides the chemical composition for each of the five materials, Palisades Weld (PW), Midland Beltline Weld (MBW), HSST Plate 02 (HSST-02), Weld 73W (73W), and the IAEA A533 grade B class 1 reference plate (JRQ).

Table 2 Chemical compositions of five RPV materials irradiated in BR2.

Material	C	Mn	Si	S	P	Cr	V	Cu	Mo	Ni	W	Al
PW	0.11	1.25	0.18	0.017	0.014	0.04	0.003	0.20	0.55	1.2	-	-
MBW	0.09	1.607	0.622	0.009	0.017	0.12	0.005	0.256	0.41	0.574	<0.01	0.015
HSST-02	0.23	1.55	0.20	0.014	0.009	0.04	0.003	0.14	0.53	0.67	<0.01	0.019
73W	0.10	1.56	0.45	0.005	0.005	0.25	0.003	0.31	0.58	0.60	<0.01	0.005
JRQ	0.18	1.42	0.24	0.004	0.017	0.12	0.002	0.14	0.51	0.84	<0.01	0.014

For each material, subsize tensile and three-point bend specimens, APT blanks, and SANS blanks were irradiated. The mechanical property specimens were tested by SCK-CEN, while the APT and SANS specimens were sent to ORNL for examination.

Brief description of APT specimen preparation and analysis procedures

Atom probe tomography needle-shaped specimens for these studies were prepared by standard electropolishing methods [15] with the use of small blanks cut from bulk materials. The electropolishing solutions were 2% perchloric acid in 2-butoxyethanol. The APT specimens were electropolished at room temperature at 15 V DC. Atom probe tomography characterizations of the surveillance specimens were performed in a Cameca Instruments LEAP® 4000 X HR local electrode atom probe. The APT analyses were performed in voltage mode with a specimen temperature of 50K, a pulse repetition rate of 200 kHz, an ion collection rate of between 0.5 and 1 ions per pulse, and a pulse fraction of 0.2. The APT characterizations of the specimens irradiated in the BR2 were performed using the LEAP 2017 atom probe, the instrument available prior to acquisition of the LEAP® 4000 X HR.

Brief description of SANS data collection and reduction

Small-angle neutron scattering (SANS) provides microstructural characterization of nanometer-sized irradiation-induced precipitates that may be inaccessible through common characterization techniques, such electron microscopy. Common irradiation-induced defects in RPV steels scatter neutrons by both nuclear and magnetic contrasts between the scattering feature and the iron matrix. The assumed non-magnetic nature of CRPs and MNPs (for which validity of this assumption has not been determined) provides the basis for SANS analysis of feature dimensions and composition. A detailed description of SANS in RPV steel application is provided in the most recent progress reports [9,16] and in the literature [17].

As previously explained, SANS measurements on the same samples were taken at both HFIR and NCNR. The data collected at HFIR were taken at the GP SANS instrument in CG2 in a saturated magnetic field of 2 Tesla oriented in the θ=0° direction at a source-sample distance of 7.077 m and two sample-target distances of 8.05 and 2.55 m. The second measurements were taken at NCNR in a saturated magnetic field of 1.3-1.5 T applied in the horizontal direction. The detector was located 1.55m from the sample and offset by 20 cm to increase the useful q range.

The raw detector count data was reduced to two irradiation-induced feature scattering cross-sections (magnetic+nuclear and nuclear) by subtracting background radiation, parasitic scattering, and scattering from an unirradiated control [18]. For the HFIR data, absolute scattering cross section $d\Sigma/d\Omega$ (q,θ) was determined for the longer sample-target geometry by normalization to an isotropic scattering cross section of a water reference sample (0.88 /cm-ster). The shorter HFIR geometry experiment lacked corresponding transmission data, requiring linear scaling of the scattering cross-section to match the longer geometry absolute scattering cross-section for the over-lapping q-range. The scaling method for the shorter

geometry has been identified as an opportunity for improvement in the future experiments. The absolute scattering cross section for the NCNR data was computed using the total beam flux incident on the sample.

Brief description of SANS data analysis

The scattering data from each sample was reduced for both the magnetic + nuclear (M+N) scattering cross-section and for the nuclear (N) scattering cross section. Note that the magnet orientation was rotated 90° in the NCNR setup vs the HFIR setup. This does not affect the data, but results in the M+N scattering cross section to be located at θ=90° in the NCNR data and θ=0° in the HFIR setup. Non-linear least square fits to the scattering cross-section data were performed under the assumptions of single spherical, non-magnetic features following a log-normal size distribution. Fitting parameters include the scattering cross section at q=0 ($\frac{d\Sigma}{d\Omega}(0)$), the magnetic to nuclear scattering ratio (M/N), and the log-normal distribution mode radius (r_m) and width parameter (β). Using both the magnetic + nuclear and nuclear scattering cross-section datasets allows for calculation of irradiation-induced feature dimensions: mean precipitate radius (r), volume fraction (f_v), and number density (N_d).

$$r = r_m e^{0.75*\beta^2}$$
$$f_v = \frac{3}{4\pi}\frac{e^{-6.75*\beta^2}}{\Delta\rho^2 r_m^3}\frac{d\Sigma}{d\Omega}(0)$$
$$N_d = \frac{9}{16\pi^2}\frac{e^{-9*\beta^2}}{\Delta\rho^2 r_m^6}\frac{d\Sigma}{d\Omega}(0)$$

where $\Delta\rho^2 = \Delta\rho_n^2 + \Delta\rho_m^2 \sin^2\theta$ is the scattering contrast between the matrix and feature scattering length densities. Non-magnetic scattering feature assumptions allow for precise determination of the magnetic scattering contrast between the iron matrix and the magnetic holes corresponding to scattering features. This allows for utilization of the relationship $\frac{M}{N} = \frac{\Delta\rho_m^2}{\Delta\rho_n^2}$ to convert the feature dimension expressions:

$$\frac{\frac{d\Sigma}{d\Omega}(0)}{\Delta\rho^2} = \frac{\frac{d\Sigma}{d\Omega}(0)}{\Delta\rho^2} * \frac{\frac{M}{N}}{\frac{\Delta\rho_m^2}{\Delta\rho_n^2}} = \frac{\frac{d\Sigma}{d\Omega}(0) * \frac{M}{N}}{\Delta\rho_m^2} \; for\ \theta = 0$$

Additional details related to SANS fitting analysis and procedures can be found elsewhere [18]. Due to the typical size distribution of precipitates, the shorter geometry experimental results encompass the entire q-range of interest and were utilized for SANS analysis. For some cases, as will be discussed below, a lack of coherent, reduced nuclear scattering cross-section data required reliance solely on the magnetic + nuclear scattering cross-section.

Comparison of HFIR and NCNR Data

First, the comparison is made on the control material results measured at both HFIR and NCNR. An example for the nuclear scattering cross section is given in Figure 1 for a high Cu (0.4%), medium Ni (0.8%) steel called LC and no Cu added (≈0.01%), medium Ni steel (0.8%) called LG. The LC results from HFIR show much higher scattering cross section at almost all q^2, although the shape of the curves is similar. The LG sample on the other hand shows that the curves from both facilities overlap until a q^2 of about 0.02, when the HFIR results increase, then level off at higher q^2. These trends are similar in the rest

of the samples. While it is possible that there could be issues with data at either or both facilities, the fact that the NCNR data aligns very well with previous control data from NCNR suggests this to be an issue with the HFIR data.

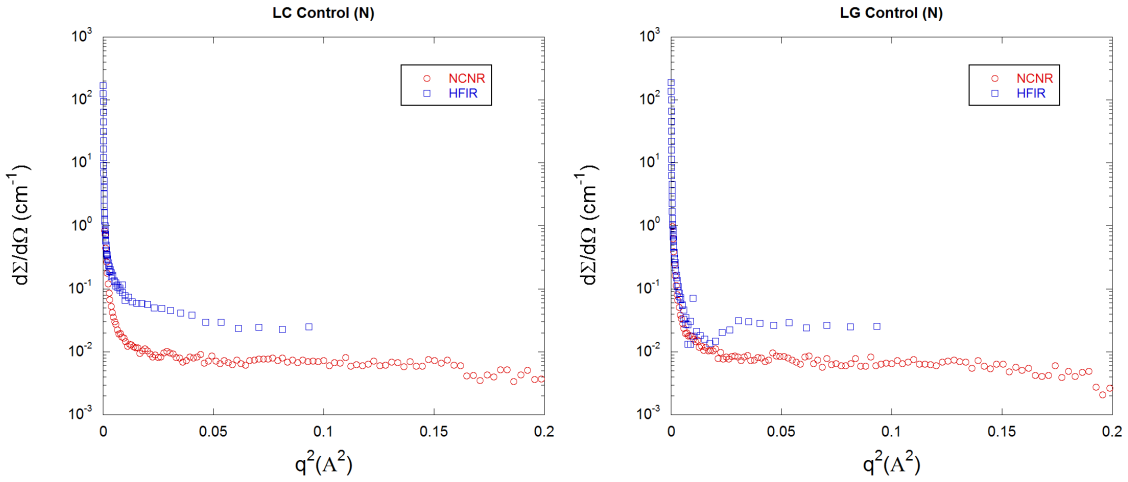

Fig. 1. Nuclear scattering cross section as a function of q^2 for two control specimens at both NCNR and HFIR.

Next, the comparison is done for the as irradiated scattering cross sections for the irradiated samples. Examples for the Nuclear (left) and Nuclear + Magnetic (right) scattering cross sections are given in Figure 2 for the Cu free, medium Ni steel LG. Similar trends as for the control samples are also present in the as irradiated samples. The curves for the HFIR data follow similarly along with the NCNR data until a q^2 of about 0.02 where the HFIR data deviates above the NCNR data. These trends are similar for the rest of the as irradiated condition, except for one steel that had overlapping curves through the entire q range for the Nuclear + Magnetic.

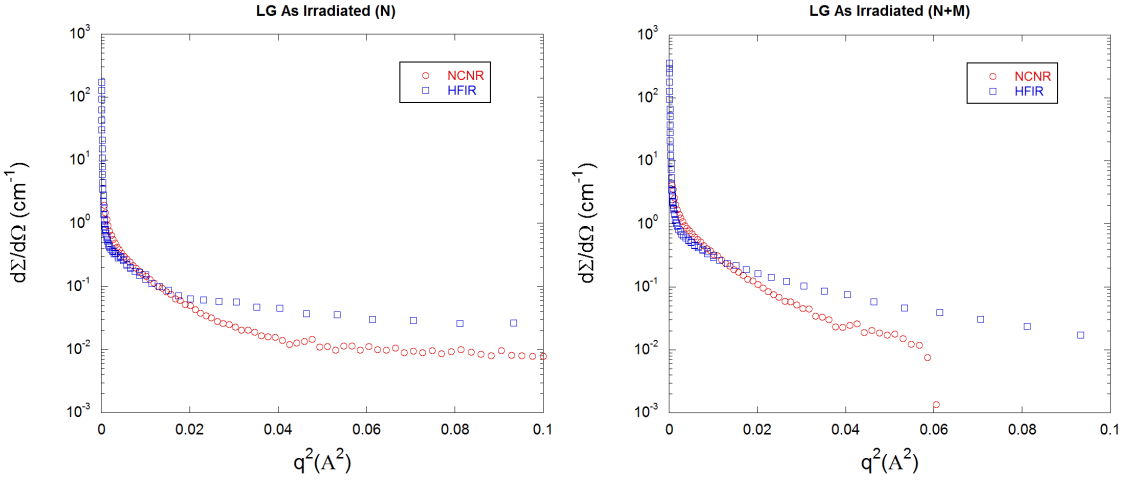

Fig. 2. Nuclear (left) and Nuclear + Magnetic (right) scattering cross sections at both NCNR and HFIR for the no Cu added, medium Ni steel (LG).

Our current hypothesis is that there was some kind of extra scattering occurring from the sample holders in the HFIR setup that results in the HFIR curves falling above the NCNR curves. To test this hypothesis, UCSB will be sending both baseline and thermally aged samples that have been previously run at NCNR to ORNL for testing at HFIR. These will be placed in the holders that are typically used by UCSB and have proven to cause no extra scattering. These samples will then be run at HFIR and

compared to the NCNR data. If the resulting curves show better agreement, then the holder design used by UCSB at NCNR will be incorporated in use at HFIR to avoid any problems in the future.

2.2 EXAMINATION OF SURVEILLANCE MATERIALS FROM THE RINGHALS REACTORS

2.2.1 Atom Probe Tomography (APT) Results

As shown in Figure 3, APT measurements of a surveillance specimen from the Unit 3 weld have revealed relatively large irradiation-induced precipitates containing nickel, manganese, silicon, and copper, with phosphorus evident in some of the precipitates. This particular specimen had been irradiated at 284°C, at a flux of 1.32×10^{11} n/cm^2 to a fluence of 6.39×10^{19} n/cm^2. Perhaps not surprisingly, the precipitate elemental concentrations are dominated by nickel and manganese atoms, with only a relatively few number of copper atoms contained within the precipitates.

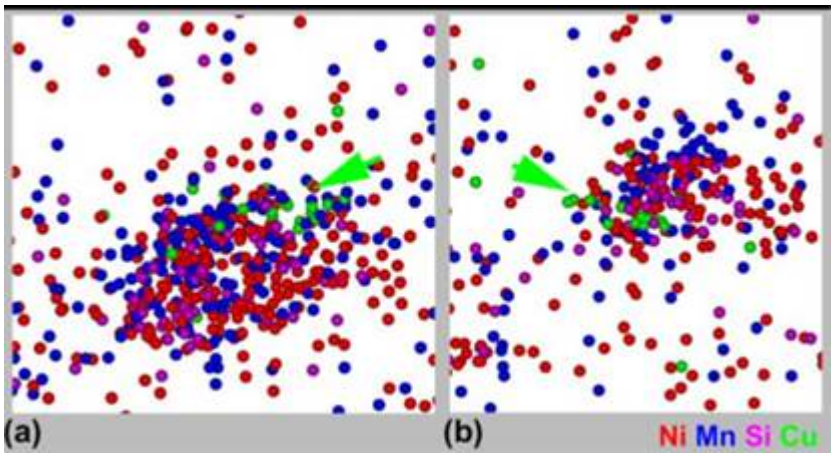

Fig. 3. (a) and (b) 1-nm-thick atom map slices through two Mn–Ni–Si precipitates in the high copper (0.08 wt %), high fluence (6.39×10^{23} n/m^2) weld metal from the Ringhals R3 Unit showing the non-uniform distribution of copper atoms.

Figure 4 (left) shows the individual atom maps for the various solutes in and associated with the precipitates in the same material irradiated to two different fluences. The atom maps illustrate the increased precipitate size associated with the higher fluence. Figure 4 (right) shows the corresponding proximity histograms for the atom maps in Figure 4 (left), providing confirmation that the precipitates are dominated by Ni, Mn, and Si, with barely a trace of Cu.

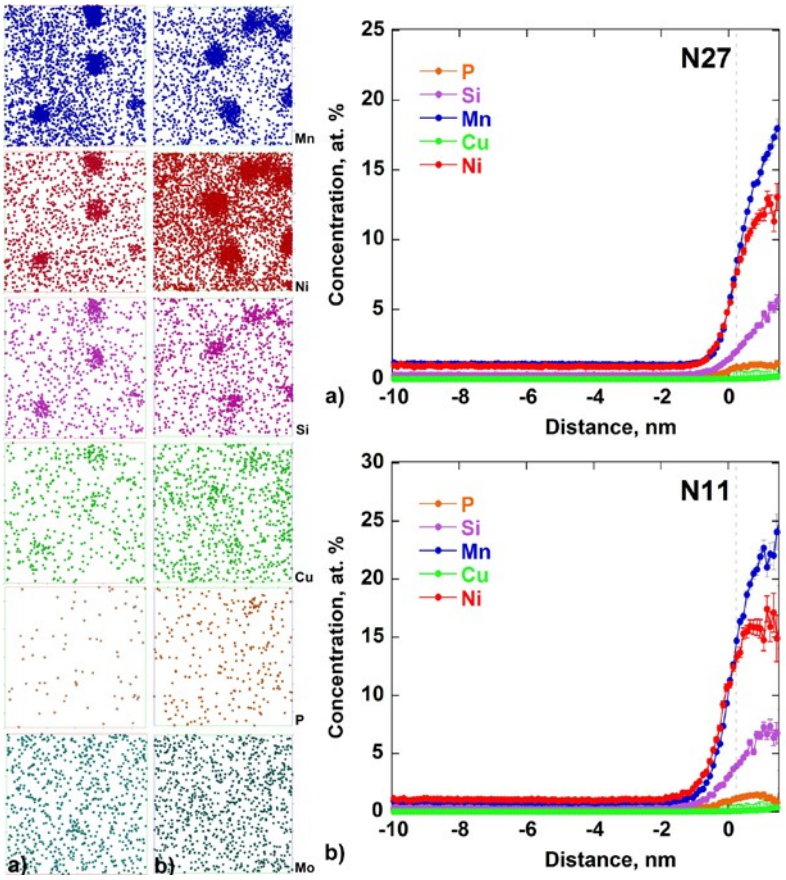

Fig. 4. Left: Atom maps of the low copper (0.05wt%) weld metal from the Ringhals R4 Unit neutron irradiated to fluences of a) 3.30 x 10^{23} and b) 6.03 x 10^{23} n m^2 (E > 1 MeV) showing the solute distribution in the precipitates; and Right: Proximity histograms showing the partitioning trends of the solute elements.

These experimental results from samples of welds used in the Ringhals R3 and R4 Units surveillance program indicate that the large shifts in the Charpy ductile-to-brittle transition temperature measurements arise from the high number density of Mn-Ni-Si precipitates. Most importantly, these results of high number densities of Mn-Ni-Si precipitates in surveillance welds also provide supporting experimental evidence for the previous results obtained from high flux, high fluence, neutron irradiations used in accelerated tests in test reactors and predicted many years ago by Odette [19]. More detailed discussions of the APT results for the Ringhals welds have been published in [20]

2.2.2 Small-Angle Neutron Scattering (SANS) Results

Chemical compositions and irradiation conditions of the Ringhals materials are provided in Table 2.3. Ringhals RPV specimens are of particular interest due to the low copper and very high nickel content, presumably providing an ideal surveillance specimen for Mn-Ni precipitate evolution.

Table 3. Chemical composition, irradiation and post-irradiation annealing conditions for SANS specimens from Ringhals Unit 3 and 4 welds.

Material	Cu	Mn	Ni	Si	Specimen	Flux (n/cm²s)	Fluence (n/cm²)	Annealing Temp/Time
Unit 3, wt%	0.08	1.46	1.58	0.21	E160	$1.47* 10^{15}$	$6.39* 10^{19}$	N/A
					E540	$1.32* 10^{15}$	$4.34* 10^{19}$	450°C/24h
Unit 4, wt%	0.05	1.35	1.66	0.14	N180	$1.49* 10^{15}$	$6.03* 10^{19}$	N/A
					N270	$1.66* 10^{15}$	$3.3* 10^{19}$	450°C/24h

Specimens E540 and N270 have undergone post-irradiation annealing (PIA) and are being studied for furthering understanding of defect recovery for potential RPV lifetime extensions. While CRP and vacancy-solute cluster recovery under PIA has been extensively studied, annealing of samples E540 and N270 may provide insight into defect recovery quantification of Mn-Ni precipitates for a more complete understanding of PIA embrittlement reduction. Figure 5 shows a clear indication of increased scattering in the two irradiated samples (E160, N180) over most of the q-range, while the annealed samples show increased scattering at very low q-values, indicative of large feature sizes.

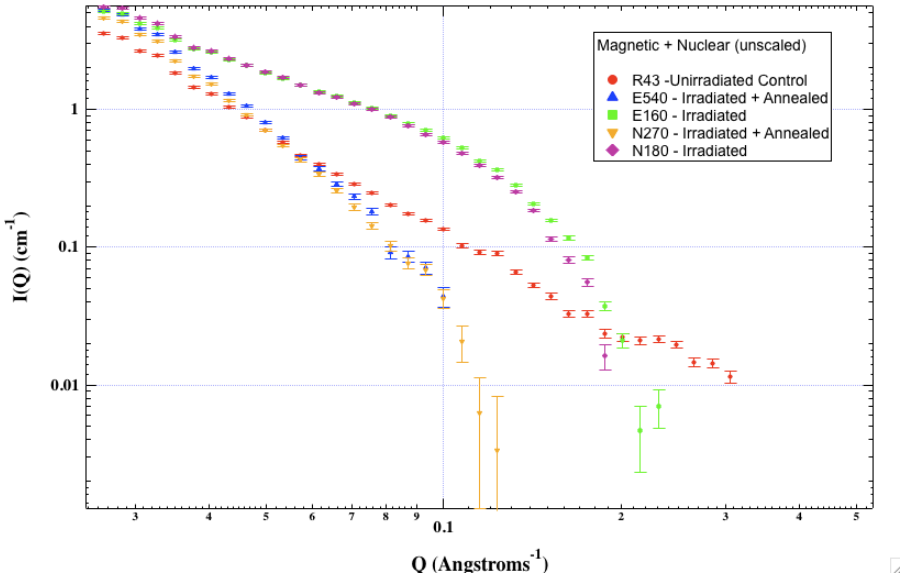

Fig. 5. Total scattering cross-section from the Unirradiated, Irradiated, and Post- Irradiation Annealed Specimens of Ringhals Units 3 and 4 welds.

Table 2.4 presents a comparison of feature dimensions between the SANS and Atom Probe Tomography (APT) analysis of specimens from Ringhals Unit 3 (E) and Unit 4 (N). SANS analysis determines a volume fraction of 0.47% and 0.38%, average radius of 1.9 and 2.2 nm, and number density of 1.38 and 0.82 $*10^{17}$ /cm^3 for E160 and N180, respectively. Both techniques show an increased average radius for the N180 specimen, although the APT results have no statistically significant difference. SANS determined a larger average radius, in both specimens, than the APT results, but this discrepancy is relatively small.

Table 4. Comparison of feature dimensions between the SANS and APT analysis of specimens from Ringhals Unit 3 (E) and Unit 4 (N).

HFIR SANS Results				APT Results		
Specimen	r (nm)	N_d (10^{17}/cm^3)	f_v (%)	Specimen	r (nm)	N_d (10^{17}/cm^3)
E160	1.9±0.26	1.4	0.47	E6	1.1±0.29	3.3
N180	2.2±0.21	0.82	0.38	N11	1.2±0.39	4.3

APT results determine the low copper specimen to have a higher number density of precipitates, while the SANS results indicate the reverse. Additionally, the SANS-determined number densities are lower for both specimens. Historic comparisons between these two techniques suggest that discrepancies in number density are within the error margins of the compared techniques. Both techniques show an increased average radius for N specimen compared to E, although the APT results have no statistically significant difference. As observed in other studies (e.g., see ref. 21), SANS determined a larger average radius than the APT results. While the error bars based on individual measurements for each technique indicate a statistically significant difference between those measured by SANS and those measured by APT, these differences are considered to be somewhat affected by differences in the specific procedures used to estimate the precipitate radii for the two techniques. In this regard, these results require further analysis. Additional coupling with Positron Annihilation Lifetime Spectroscopy (PALS) analysis may provide further insight into the feature dimension and composition differences between these two samples. Additionally, SANS analysis of E540 and N270 prior to annealing may provide further insight into the fluence-dependence of precipitate evolution in low copper, high nickel RPV steels.

Post-irradiation annealed specimens, E540 and N270 (the lower fluence samples) were analyzed over the accessible low q- range 0.026-0.053 Å^{-1}, corresponding to large feature sizes attributed to precipitate coalescence. Annealing results in a decrease in volume fraction from about 0.43±0.05% to 0.04±0.0175% and a 1000x reduction in the number density of precipitates

In addition to performing SANS measurements at HFIR, UCSB just recently completed SANS measurements at NCNR. The results are very preliminary and future evaluations are necessary. On average, the SANS results of the RPV materials irradiated in UCSB ATR-1 showed about 70% of the volume fraction that were seen in APT. This suggests that the absolute calibration may be off in the experiment and it will be investigated in more detail. The preliminary results on Ringhals specimens are summarized in Table 2.5.

Table 5. HFIR and preliminary NCNR SANS results on two Ringhals specimens.

Specimen	r (nm)		N_d (10^{17} cm^{-3})		f_v (%)	
	HFIR	NCNR	HFIR	NCNR	HFIR	NCNR
E160	1.9	1.8	1.4	3.6	0.47	0.59
N180	2.2	1.9	0.8	2.6	0.38	0.46

Although there are some slight differences between the two results, the trends match up very well. Both the NCNR and HFIR data show that the E160 sample has a smaller average radius, larger number density and larger volume fraction of precipitates. The NCNR shows slightly smaller and more numerous clusters though. This agreement is encouraging that the issues with the HFIR results on the ATR-1 materials are not caused by the beamline or data reduction procedures. It should be pointed out that the Ringhals samples were 1cmx1cm squares, while the ATR-1 materials investigated at HFIR were 3mm discs. Because the ATR-1 materials were so much smaller, the room for error in terms of the beam potentially hitting part of the holder was much smaller. Again, this is why we will run control and aged materials at HFIR using the NCNR holders to determine if the issues were caused by the holders.

2.3 EXAMINATION OF SURVEILLANCE MATERIALS FROM THE R. E. GINNA REACTOR

2.3.1 Atom Probe Tomography (APT) Results

Atom probe experiments were performed for both the forging and the weld at all three fluences noted above in Section 2.1. Figure 6 shows an atom map for the forging irradiated to 1.7×10^{19} n/cm^2. The specimen examined contained only 0.05 wt% Cu and the atom map indicates precipitates with Ni, Mn, Si, but no Cu enrichment. The atom map of Cu on the right of Figure 6 shows no evidence of Cu clustering relative to the distinct precipitates in the left hand map. Atom probe maps of the forging specimens at the higher fluences showed similar results but also with some Cu-enriched precipitates in the matrix and preferential precipitation of Cu-enriched precipitates and P segregation to dislocations.

These latter observations of Cu enrichment were only observed in samples with somewhat higher Cu content in the samples examined than the overall bulk content.

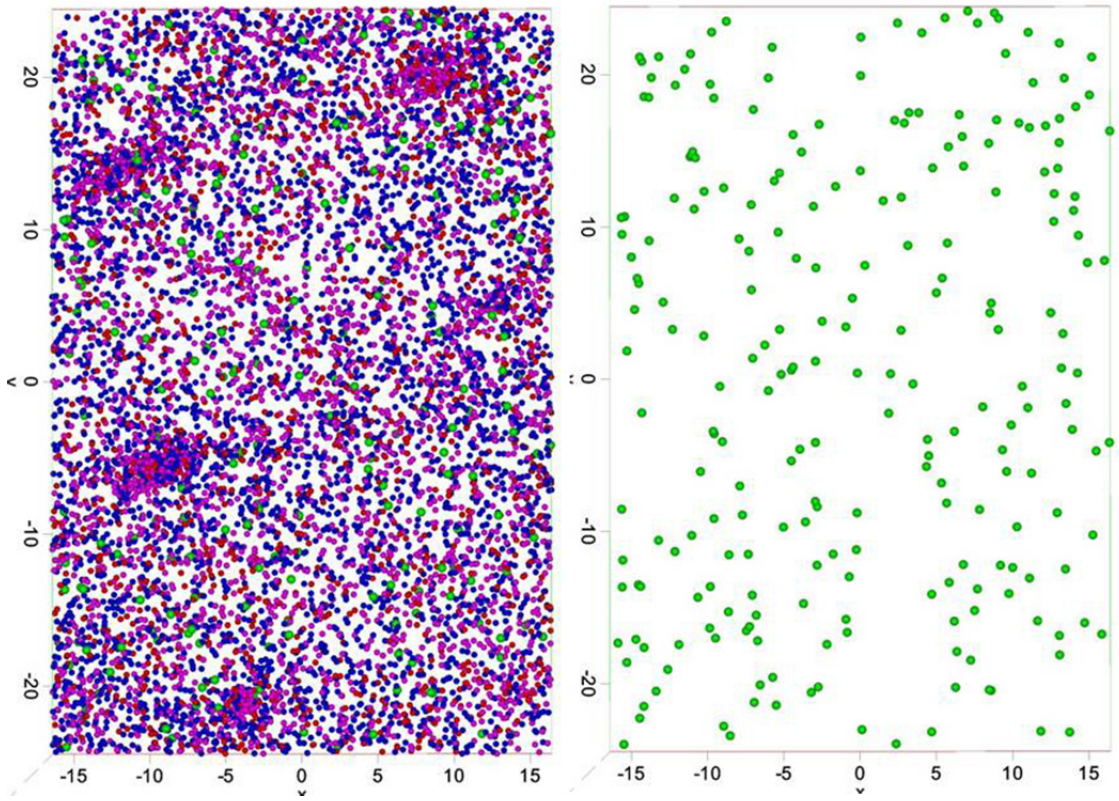

Fig. 6. Atom tomography maps of the Ginna Reactor forging irradiated to 1.7×10^{19} n/cm^2 showing NiMnSi precipitates in the left hand map, while the right hand atom map indicates no Cu clustering associated with those precipitates.

The Ginna weld metal samples contain about 0.23 wt% Cu and the precipitates shown in Figure 7 reveal the strong enrichment of Cu as well as Ni, Mn, and Si. The higher Cu weld also exhibited ultrafine CuNiMnSi and P-enriched precipitates and P segregation to the dislocations.

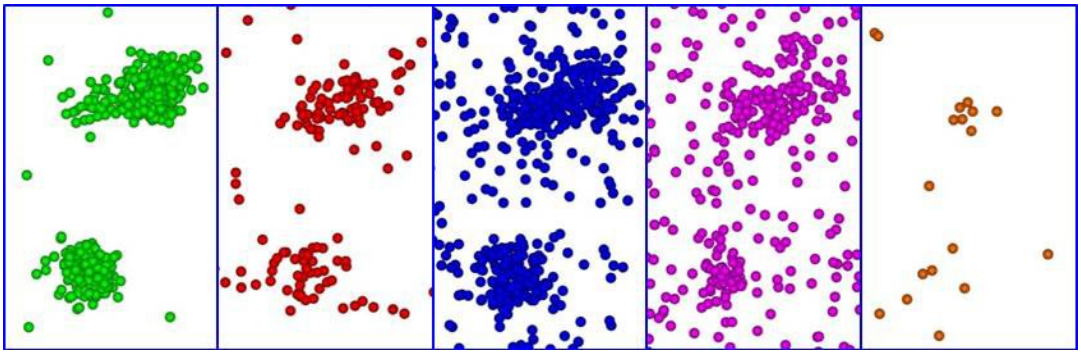

Fig. 7. Atom maps showing Cu-enriched precipitates that include Ni, Mn, and Si.

Similar behavior was observed in the intermediate fluence and high fluence weld specimens. The size and number densities of the Cu-enriched precipitates were much smaller in the forgings due to the lower Cu contents. Moreover, there was a trend for the number densities to increase with higher fluence. A preliminary observation from this and other APT experiments is the irradiation-induced copper-enriched precipitates from surveillance and test reactor irradiations have nominally the same characteristics. A graph of bulk Cu level in the APT samples (atomic %) vs the precipitate number density for the Ginna surveillance materials shows that a polynomial curve fit describes the results (six data only) well and, moreover, the intercept of the curve suggests that the minimum Cu level in the Ginna materials for forming Cu-enriched precipitates is 0.046 at.% Cu.

2.3.2 Small-Angle Neutron Scattering (SANS) Results

Small-angle neutron scattering was performed only on weld metal specimens from The R. E. Ginna reactor due to the unavailability of an unirradiated specimen of forging material that is necessary for SANS measurements as described in the background section. Table 2.6 summarizes the irradiation conditions of SANS specimens and corresponding changes in mechanical properties from surveillance test data and recent hardness measurements [22].

Table 6. Irradiation conditions and corresponding mechanical properties of Ginna weld metal for SANS studies.

Weld	Fluence (10^{19} n/cm^2)	Flux (10^{10} n/cm^{2}s)	ΔTT_{30} (°C)	Avg. μH	ΔYS (MPa)
W30	1.69	8.12	83	266.4	100
H39	3.64	6.62	118	238.8	103-138
H48	5.8	5.92	120	277.4	207

As seen in Figure 8, specimen H48 scattering data does not follow the expected trends for SANS scattering and is not accessible through the fitting analysis procedure, suggesting inconsistencies in matrix chemistry between the un-irradiated control and H48. Speculations were raised in [22] over whether H48

was properly identified as weld metal due to minimal differences in hardness between the H48 forging and weld metals. Further analysis of this sample for composition and metallurgical identification may resolve this issue for future work on Ginna samples. Comparisons in this progress report will focus on W30 and H39 specimens of weld metal.

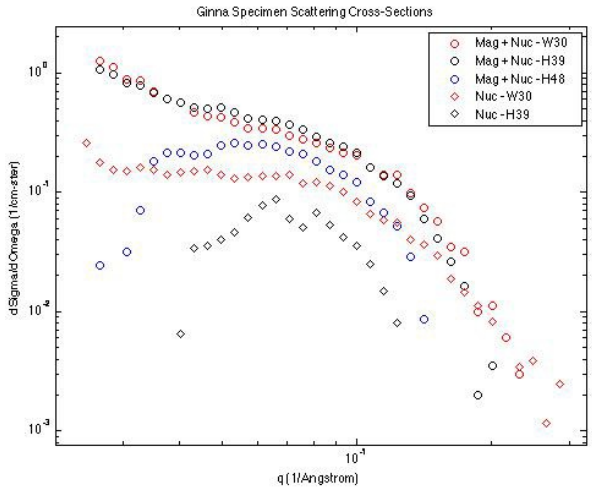

Fig. 8. Total and nuclear normalized scattering cross-sections for Ginna weld specimens at three fluences.

To provide a comparison between W30 and H39, the fitting analysis was performed for the q- range 0.07-0.2 $Å^{-1}$. While W30 scattering cross-section data was available over this range for both magnetic + nuclear and nuclear, Figure 8 shows the very limited range of available nuclear scattering data for H39, which restricted fitting to only the magnetic + nuclear scattering over several incremental fixed values of M:N scattering ratio. The correlated changes in calculated volume fraction and number density of scattering features are presented in Figure 9. The M:N scattering ratio for H39 is expected to increase in comparison to W30 due to coalescence and scattering feature composition changes consistent with the higher fluence regime. A M:N ratio of 2 has been chosen for the remaining comparison between these specimens. This selection is supported by the slightly higher volume fraction that corresponds to the slight increase in embrittlement seen in Table 2.6.

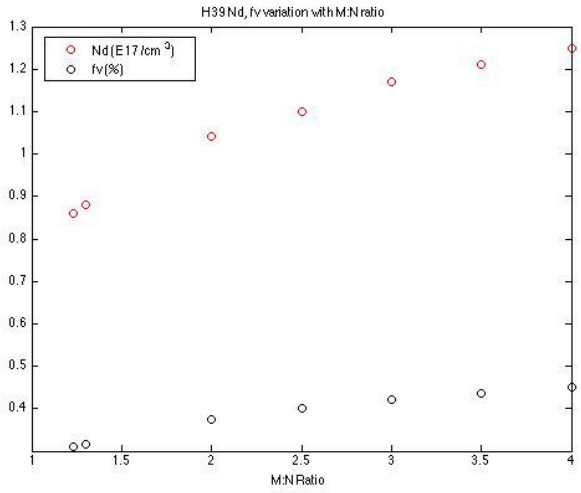

Fig. 9. H39 feature number density and volume fraction varying M:N ratio from 1.3-4.

Figure 10 shows the close match between the fitting routines and the three curves of interest for the Ginna SANS analysis, as well as providing the corresponding parameters.

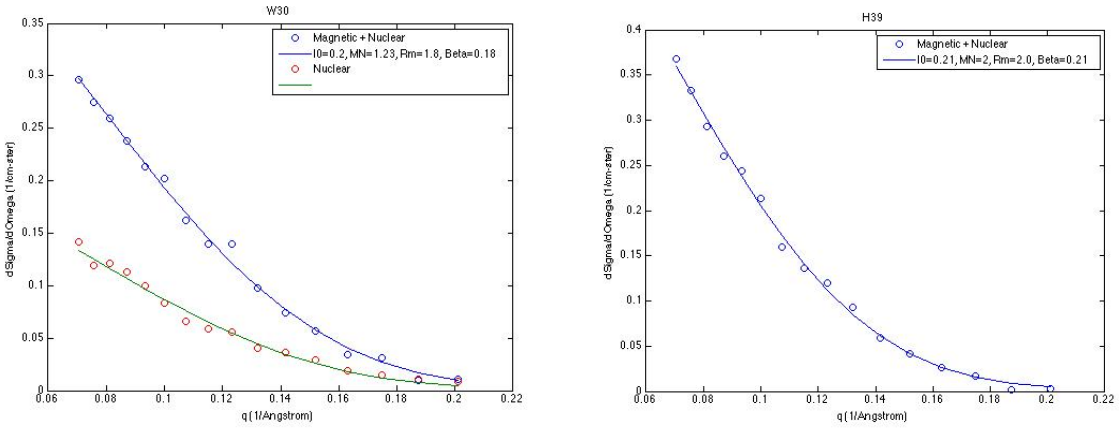

Fig. 10. Data and respective fits for W30 (left) and H39 (right) weld specimens.

An increase in the average radius and volume fraction and decrease in number density, as seen for both APT and SANS analysis in Table 2.7, provides further indication of coalescence evolution at higher fluence. APT results signify smaller average radius and larger number densities than SANS (similar to the results for the Ringhals samples), which may be a result of higher sensitivity to smaller clusters and precipitates; SANS is limited to scattering features greater than 4-5 Å. Overall, there is sufficient agreement between the two supporting microstructural characterization techniques and hardness measurements. Further work will include PALS as a third technique for feature dimension justification and for resolution of the M:N ratio for H39.

Table 7. Comparison of SANS and APT results for Ginna weld specimens.

	SANS			APT	
Weld	r (nm)	N_d (10^{17}/cm^3)	f_v (%)	r (nm)	N_d (10^{17}/cm^3)
W30	1.8±0.21	1.26	0.33	0.93±0.17	2.8
H39	2.0±0.25	1.05	0.37	1.1±0.31	1.7

2.4 EXAMINATION OF TEST REACTOR MATERIALS FROM THE BR-2 REACTOR

2.4.1 Atom Probe Tomography (APT) Results1

APT examinations were performed on four of the materials using the LEAP 2017 atom probe. The maximum separation envelope method with a 10 atom cut off was used for all precipitate analyses. Solute segregation at precipitate-matrix interfaces was examined with proximity histograms. Some examples of the APT maps and proximity histograms will be presented here with brief discussion of the results.

Figure 11 shows atom maps for HSST Plate 02, with Cu, Ni, Mn, Si, and P presented. Inspection of the maps reveals that each of those five solutes are observed in the precipitates, although P was primarily observed in the vicinity of the precipitates as shown in the proximity histogram of Figure 11. No dislocations were encountered in this sample.

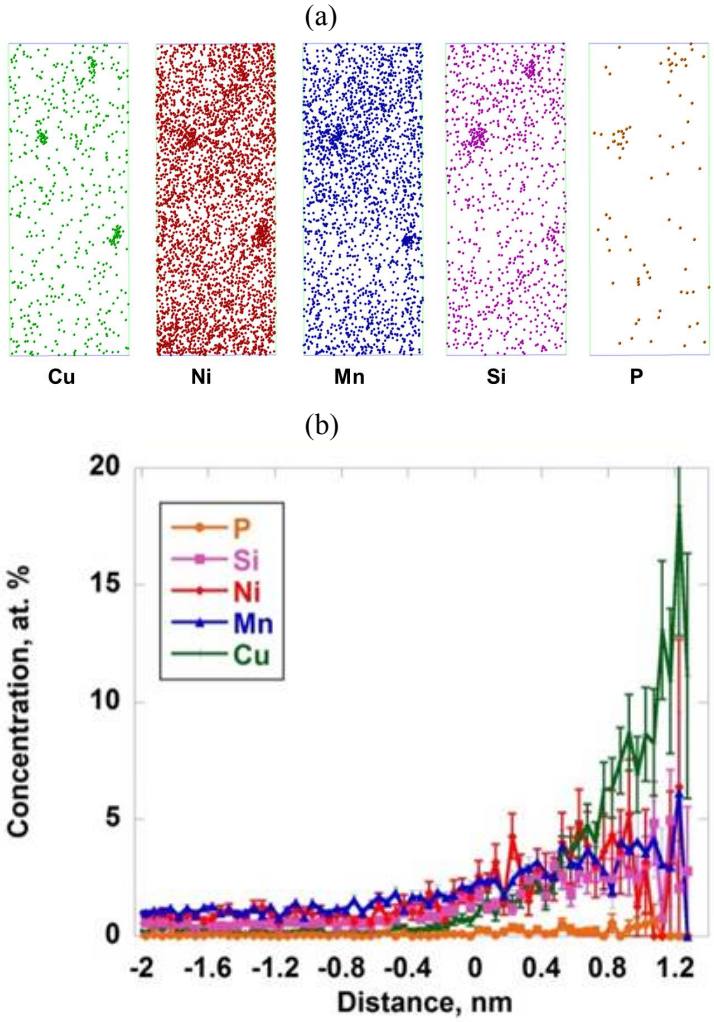

Fig. 11. APT results of HSST Plate 02 irradiated to 7.2×10^{19} n/cm^2 in the BR-2 showing (a) atom maps for individual solutes.

Figure 12 shows atom maps and a proximity histogram for the Midland Beltline Weld irradiated to 6.45×10^{19} n/cm^2. This weld is a high Cu weld (0.27 wt%), and the histogram shows the elevated concentration of Cu in the precipitates compared with the case of HSST Plate 02 with a Cu content of 0.14 wt%. The Midland weld also exhibited significant segregation of Si, P and Mn to dislocations.

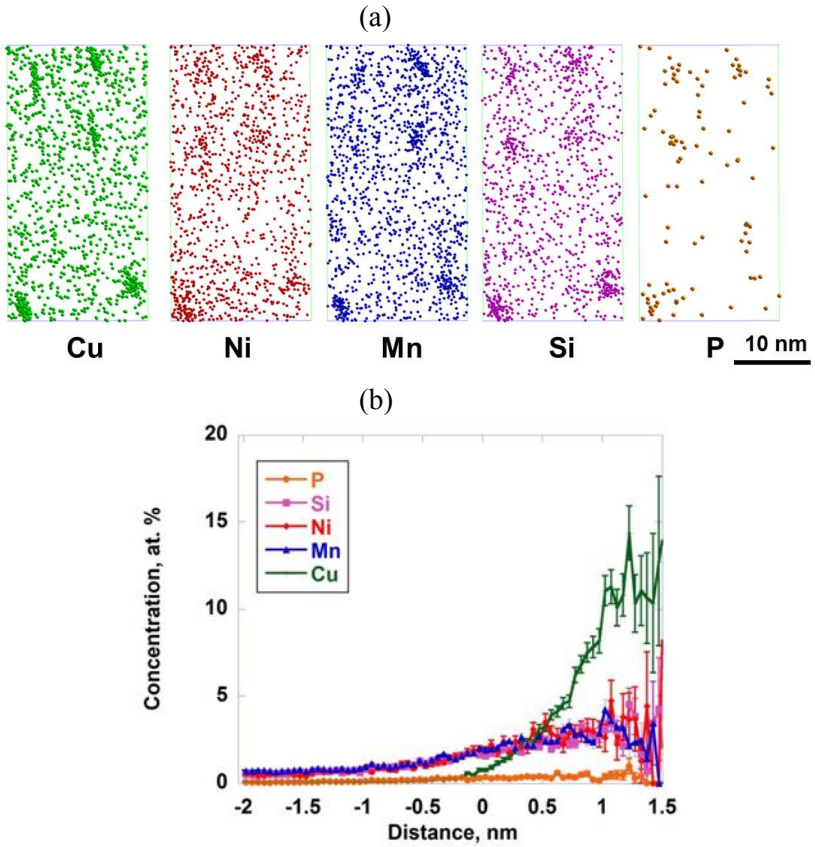

Fig. 12. APT results of Midland Beltline Weld irradiated to 6.45×10^{19} n/cm^2 in the BR-2 showing (a) atom maps for individual solutes, and (b) proximity histogram showing the distribution of solutes relative to the precipitate. Note the high elevated concentration of Cu in the precipitate.

For the Midland weld results, the precipitate radius of gyration is about the same as determined for the same weld irradiated in the Ford Research Reactor at a flux level almost two orders of magnitude lower and to a fluence about half of the BR2 irradiation. On the other hand, the average number density of precipitates in the BR2 case is about 2.5 times greater than that in the lower flux irradiation, although the number densities determined were highly variable.

Those results contrast, however, with the results for HSSI Weld 73W, a very high Cu weld (0.31 wt%) also irradiated to 6.45×10^{19} n/cm^2 ; the precipitate sizes are, again, about the same, but the number densities are also about the same for both the low and high flux cases.

In the case of the Palisades Weld irradiated to fluences of 6.45 and 10.5×10^{19} n/cm^2 in the BR2, there were no significant differences in the sizes or number densities of the Cu-enriched precipitates for both BR2 fluences and when compared with lower flux irradiations in the Ford Reactor to 1.4 and 3.4×10^{19} n/cm^2.

2.4.2 X-Ray Diffraction (XRD), Small Angle X-Ray Scattering (SAXS) and Atomic Pair-Distribution Function (PDF) Results

In addition to APT, specimens irradiated in the BR2 reactor were sent to the National Synchrotron Light Source (NSLS) at the Brookhaven National Laboratory (BNL) for an exploratory study to assess ability of an available suite of x-ray diffraction-based techniques to characterize radiation defects in RPV steels. High-resolution x-ray diffraction (XRD), small angle x-ray scattering (SAXS) and atomic pair-distribution function (PDF) measurements have been just recently completed at the NSLS using the high-energy x-rays available at beamline X17A and preliminary results are discussed in this section.

Figure 13 shows a schematic of the beamline at X17A with all optical and detector elements labeled for reference. For both sets of measurements an a-Si pixel array detector (2048x2048 pixels) was mounted orthogonal to the beam path, centered on the beam.

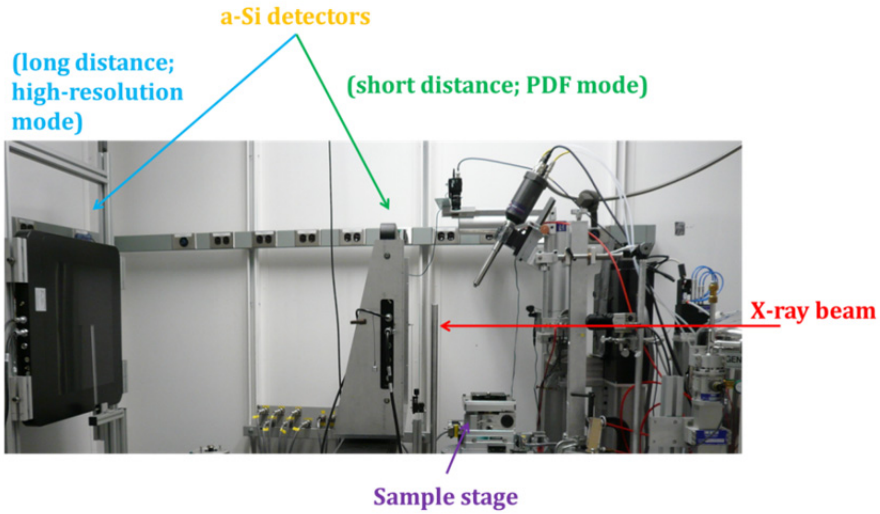

Fig. 13. Photo of X17A endstation at the National Synchrotron Light Source.

The sample-to-detector distance and tilt of the detector relative to the beam were refined using a Nickel NIST powder standard. At X17A the wavelength of the incident x-rays is 0.1839 (67.42 keV). The sample-to-detector distances (SDD's) were calculated to be ~200 mm and ~1560 at the near and far detectors, respectively. The larger SDD (with smaller scattering vector, Q) was used for the SAXS and Rietveld analysis of the XRD patterns, while the short distance was used for the PDF analysis (wider Q-space). Multiple patterns were collected on 2-3 different parts of each sample with count times adjusted to maximize the signal and to be away from the saturation limit of the detector. Typical count times were 0.5-1 sec (depending on the sample), and each image consisted of 100 individual exposures (to maximize signal to noise ratio). All raw .tiff images were background corrected by subtracting a dark current image (collected at an identical rate without exposing the detector to x-rays) and masking regions of the images with noticeable artifacts (beam stop, shadowing and edge of the detector). The corrected two-dimensional images were then averaged together and radially integrated, excluding the area in which the beamstop arm shadowed the scattered beam, to obtain the one-dimensional powder diffraction pattern.

All samples showed powder-like patterns with no obvious preferred orientation. Figure 14 shows the two-dimensional SAXS/XRD detector patterns for the Midland (a) unirradiated and (b) irradiated samples. Figure 15 shows the reduced one-dimensional diffraction patterns for these two samples, with the phases included for reference. The irradiated samples have more intense scattering components both in the ferrite and secondary phases. The unknown phase in Figure 15 (with arrows), could potentially be

attributed to the CuNiMnSi precipitates with a different unit cell (still needs to be verified based on the chemistry and irradiation conditions of this particular sample).

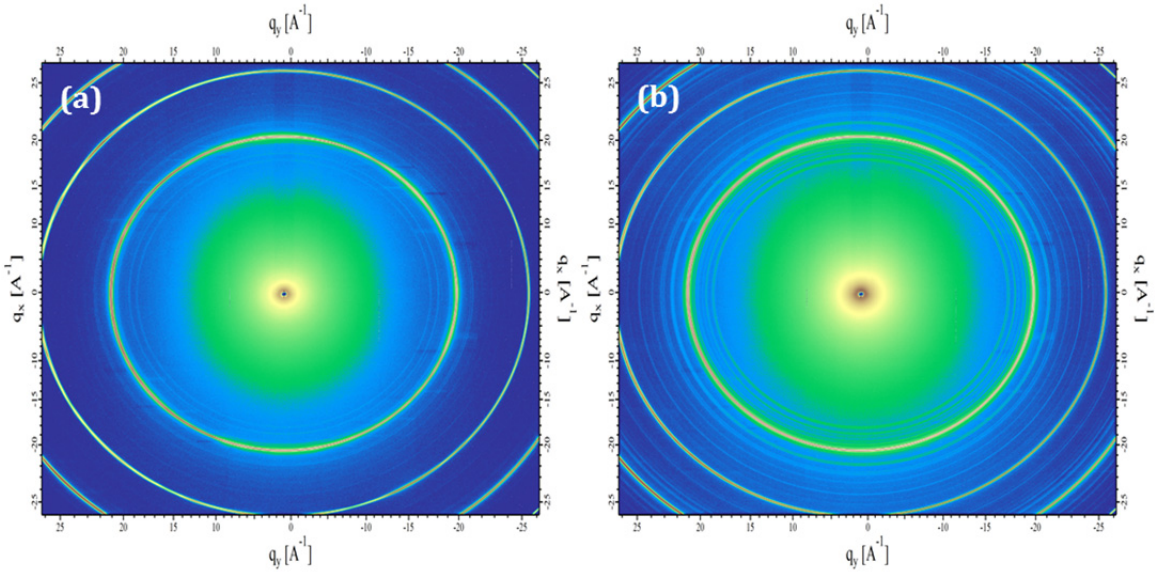

Fig. 14. Two dimensional detector images of (a) unirradiated and (b) irradiated Midland samples.

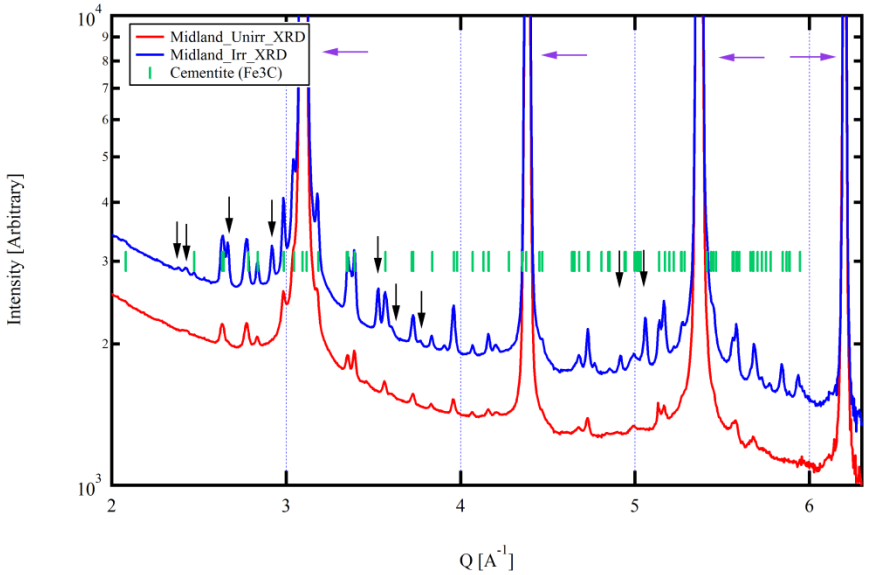

Fig. 15. XRD patterns for the Midland samples. The peaks attributable to the cementite (Fe_3C) phase, alpha iron (purple arrows) and unknown phase (black arrows) are included for reference.

The pair distribution function (PDF) analysis, is another powerful x-ray technique used to determine the distribution of distances between atoms in a volume. This technique is independent of the material's crystalline structure and facilitates the determination of atomic distances in crystalline materials, non-crystalline (i.e. disordered and amorphous materials) and nano materials. The PDF method involves a direct Fourier transformation of the diffraction pattern and gives the probability of finding any two atoms at a given interatomic distance. Figure 16 shows the PDFs determined for the Midland samples. Subtle differences in the local structure are apparent between the control (unirradiated) and

irradiated sample, while extraction of the bondlengths, phases and atomic information on the precipitates could be pursued in the future.

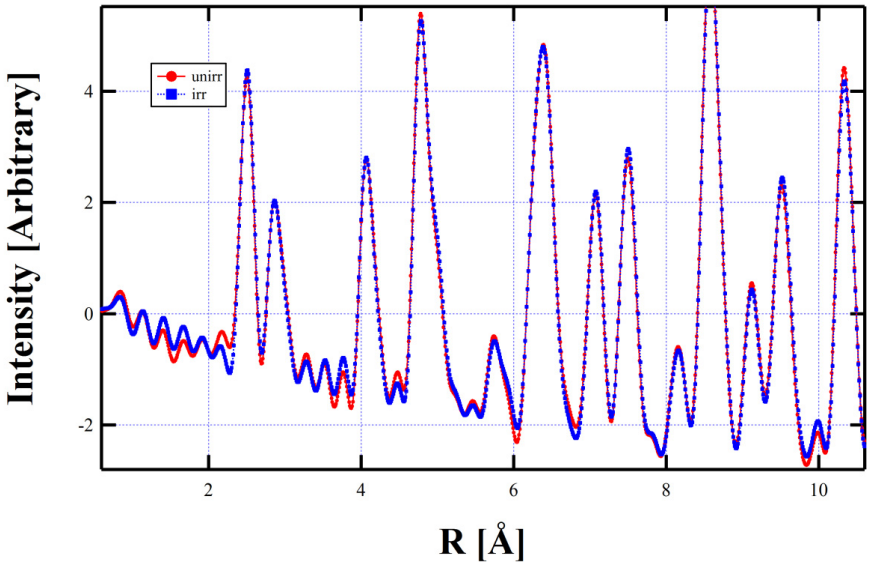

Fig. 16. PDF of the Midland unirradiated (red) and irradiated (blue) samples with a window that highlights some of the subtle atomic changes upon irradiation.

Figure 17 shows the XRD patterns collected for all samples measured during the beamtime. Various differences were observed between the unirradiated and irradiated samples including changes in the background, peak heights and broadening/sharpening of the cementite precipitates. A slight copper component was also observable in some samples (small peak at ~3.50 $Å^{-1}$). A full Rietveld analysis is underway to determine quantitative changes in the structure, phase and composition.

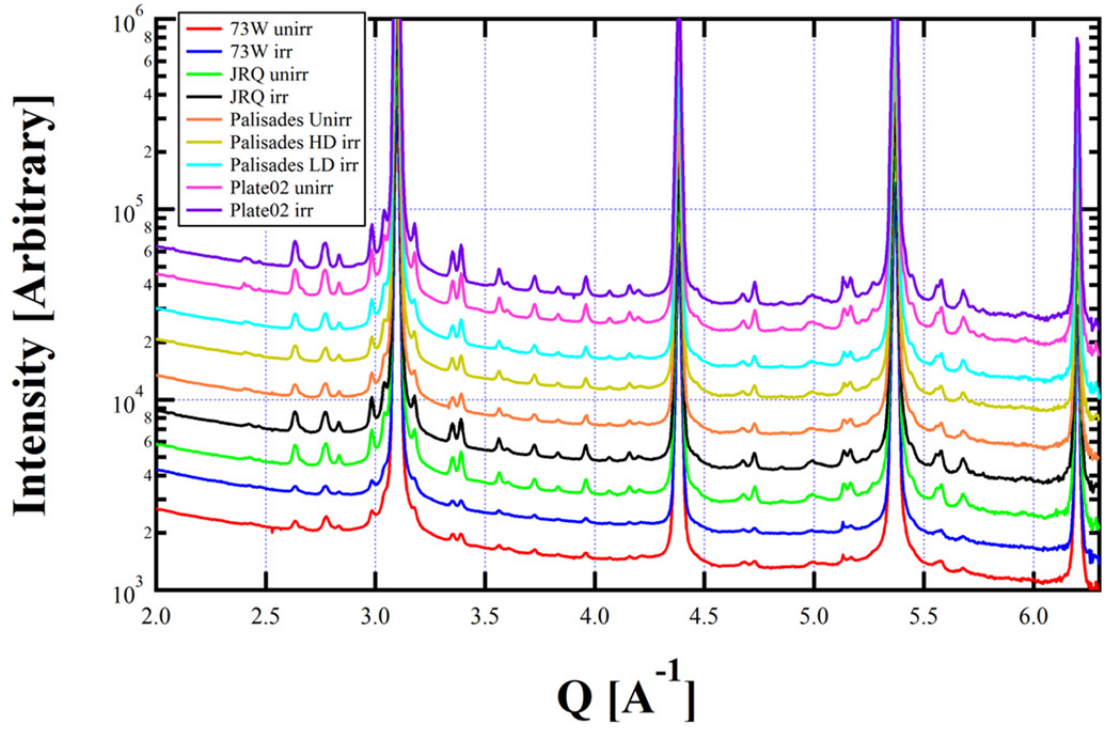

Fig. 17. XRD patterns for all RPV samples.

Figure 18 shows the background corrected SAXS patterns for the two different sample sets shown in Figure 17. Visible differences in the SAXS patterns are observable and indicative of different feature sizes. Fitting the SAXS intensity as a function of Q is planned to determine the changes in the feature size.

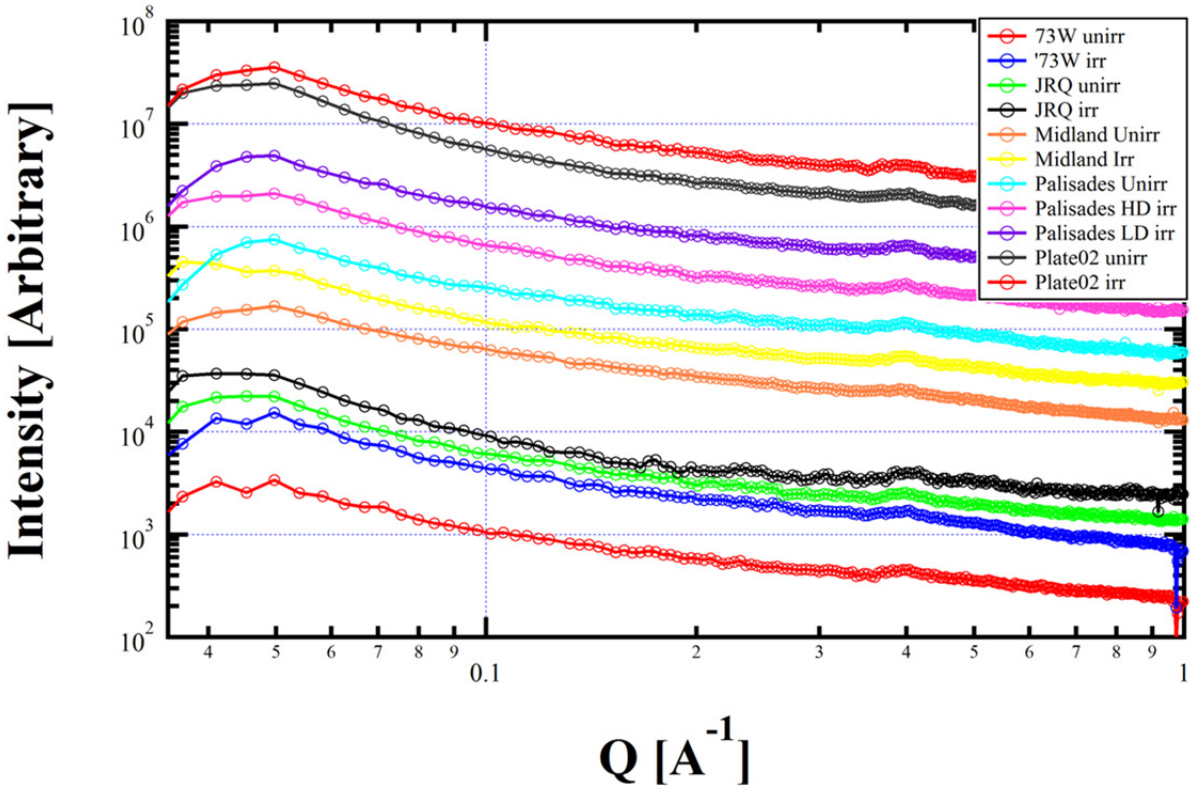

Fig. 18. Background corrected SAXS (air and Kapton scatter removed) patterns for all samples measured.

3. SUMMARY AND CONCLUSIONS

The primary objective of the LWRSP RPV task is to develop robust predictions of transition temperature shifts (TTS) at high fluence (φt) to at least 10^{20} n/cm^2 (>1 MeV) pertinent to plant operation of some pressurized water reactors (PWR) for 80 full power years. The RPV task of the LWRS Program is working with various organizations to obtain archival surveillance materials from commercial nuclear power plants to allow for comparisons of the irradiation-induced microstructural features from reactor surveillance materials with those from similar materials irradiated under high flux conditions in test reactors. Small pieces of surveillance specimens from the Ringhals nuclear plants, Units 3 and 4, previously tested Charpy impact surveillance specimens of forging, weld metal, and heat-affected-zones from the R. E. Ginna Nuclear Plant, and four materials irradiated in the BR-2 test reactor have been examined with atom probe tomography, small-angle neutron scattering, high-resolution x-ray diffraction, small angle x-ray scattering, and atomic pair-distribution function measurements.

The APT and SANS analysis of the Ringhals welds showed high number densities of Mn-Ni-Si precipitates in surveillance welds that provides supporting experimental evidence for the previous results obtained from high flux, high fluence, neutron irradiations used in accelerated tests in test

reactors. Among two techniques, the SANS-determined number densities are somewhat lower than APT numbers. Historic comparisons between these two techniques suggest that discrepancies in number density are within the error margins of the compared techniques. In anticipation of a large number of SANS specimens from the UCSB ATR-2 experiment, SANS measurements on Ringhals weld specimens were performed at NCNR where a large database of SANS data have been established previously by UCSB. While results at NCNR are preliminary at this point, the comparison of radius, number density, and volume fraction of precipitates derived at NCNR and HFIR are in general agreement. Despite this general agreement, the comparison has also revealed some deficiency in experimental set-up at HFIR that requires improvement. A series of experiments are designed and scheduled to address this deficiency using UCSB model alloys previously measured at NCNR. For the APT and SANS analyses of the Ginna materials, there is sufficient agreement between the two supporting microstructural characterization techniques (APT and SANS) and hardness measurements, but scatter in precipitate number density measurements for both techniques is rather high. From the examinations of four RPV materials irradiated in the high flux BR2 test reactor, APT characterizations of the higher flux, higher fluence irradiations have not revealed any significant differences in the size and number density of the Cu-enriched precipitates. In addition to APT, specimens irradiated in the BR2 reactor were sent to the National Synchrotron Light Source (NSLS) at the Brookhaven National Laboratory (BNL) for an exploratory study to assess the ability of an available suite of x-ray diffraction techniques to characterize radiation defects in RPV steels. High-resolution x-ray diffraction (XRD), small angle x-ray scattering (SAXS) and atomic pair-distribution function (PDF) measurements have been just recently completed at the NSLS using the high-energy x-rays available at beamline X17A and preliminary results indicate potential for future evaluation of these techniques to characterize irradiation-induced defects in RPV steels.

4. REFERENCES

1. Eason, E. D., Odette, G. R., Nanstad, R. K., and T. Yamamoto, **"A Physically Based Correlation of Irradiation-Induced Transition Temperature Shifts for RPV Steels,"** Journal of Nuclear Materials, Volume 433, Issues 1-3, 2013, pp. 240-254.

2. Nanstad, R. K. and Odette, G. R., "**Reactor Pressure Vessel Issues for the Light-Water Reactor Sustainability Program**," pp. 1667-1676 in *Proceedings of the 14th International Conference on Environmental Degradation of Materials in Nuclear Power Systems Water Reactors,* ANS, LaGrange, Illinois, 2010..

3. Odette, G. R. and Nanstad, R. K., **"Predictive Reactor Pressure Vessel Steel Irradiation Embrittlement Models: Issues and Opportunities,"** *J. Metals,* 61, 7, July 2009.

4. Miller, M.K. and Russell, K.F., **"Embrittlement of RPV steels: An atom probe tomography perspective,"** J. of Nucl. Matls, 371 (1–3) (2007), p. 145

5. Nanstad, R. K. and Odette G. R., **"Reactor Pressure Vessel Task of Light Water Reactor Sustainability Program: Milestone Report on Materials and Machining of Specimens for the ATR-2 Experiment,"** ORNL/LTR-2011/413, Oak Ridge National Laboratory, January 2011.

6. Nanstad, R. K., Odette, G. R., Yamamoto, T., and Sokolov, M.A., **"Post-irradiation Examination Plan for ORNL and University of California Santa Barbara Assessment of UCSB ATR-2 Irradiation Experiment,"** ORNL/LTR-2013/598, Oak Ridge National Laboratory, December 2014.

7. Nanstad, R. K., **"Reactor Pressure Vessel Task of Light Water Reactor Sustainability Program: Assessment of High Value Surveillance Materials,"** *ORNL/LTR-2011/172*, Oak Ridge National Laboratory, June 2011.

8. Nanstad, R. K., **"Reactor Pressure Vessel Task of Light Water Reactor Sustainability Program: M3LW-12OR0402012 - Letter Report on Metallurgical Examination of the High Fluence RPV Specimens From the Ringhals Nuclear Reactors,"** *ORNL/LTR-2012/113*, Oak Ridge National Laboratory, March 2012.

9. Sokolov, M. A., Littrell, K. C., and Nanstad, R. K., **"Reactor Pressure Vessel Task of Light Water Reactor Sustainability Program: Milestone M3LW-13oR042012, Report on Small-Angle Neutron Scattering Experiments of Irradiated RPV Materials,"** ORNL/TM-2012/630, Oak Ridge National Laboratory, December 2012.

10. Nanstad, R. K., **"Reactor Pressure Vessel Task of Light Water Reactor Sustainability Program: Level 3 Milestone (M3W-12OR0402014) - Progress Report on Examinations of the Surveillance Specimens from the Ginna and Palisades Reactors,"** *ORNL/LTR-2012/335*, Oak Ridge National Laboratory, August 2012.

11. U.S. Nuclear Regulatory Commission, **"Radiation Embrittlement of Reactor Vessel Materials,"** Regulatory Guide 1.99, Revision 2 (Washington, D.C.: U.S. Nuclear Regulatory Commission, 1988).

12. P. Efsing, C. Jansson, T. Mager, and G. Embring, **"Analysis of the Ductile-to-Brittle Transition Temperature Shift in a Commercial Power Plant with High Nickel Containing Weld Material,"** J. ASTM Int., Vol. 4, No. 7, Paper ID JAI100719, 2007, Available online at www.astm.org.

13. Rosier, B. A., **"Analysis of Capsule N from the R. E. Ginna Reactor Vessel Radiation Surveillance Program,"** *WCAP-17036-NP*, Westinghouse Non-Proprietary Class E, September 2010.

14. Lucon, E., **"Irradiation of Heavy-Section Steel Irradiation (HSSI) Program Specimens in the BR2 Reactor: the FRISCO-R Experiment,"** SCK•CEN-R-4325, April 2006.

15. M.K. Miller, A. Cerezo, M.G. Hetherington, G.D.W. Smith, *Atom Probe Field Ion Microscopy*, Oxford University Press, Oxford, UK, 1996. p. 476.

16. Nanstad, R. K., Sokolov, M. A., Miller, M. K., Williams, G.T., and Littrell, K. C., **"Microstructural Examinations of Reactor Pressure Vessel Surveillance and Test Reactor Irradiated Materials,"** ORNL/TM-2013/462, Oak Ridge National Laboratory, September 2013.

17. Sokolov, M.A., Spooner, S., Odette, G.R., Wirth, B.D., and Lucas, G.E., **"SANS Study of High-Copper RPV Welds in Irradiated and Annealed Conditions,"** pp. 333-345 in Effects of Radiation on Materials: 18th International Symposium, ASTM STP 1325, R.K. Nanstad, M.L. Hamilton, F.A. Garner, and A.S. Kumar, Eds., 1999.

18. Glade, S.C., Wirth, B.D., Odette, G.R, and Kumar,P.A., **" Positron annihilation spectroscopy and small angle neutron scattering characterization of nanostructural features in high-nickel model reactor pressure vessel steels,"** J. of Nucl. Materls, 351 (13) (2006) p.197.

19. Odette, G.R., **"Microstructural Evolution During Irradiation,"** p. 137 in *MRS Symp. Proc. 373,* Materials Research Society (1995).

20. M.K. Miller, K.A. Powers, R.K. Nanstad, and P. Efsing, **"Atom probe tomography characterizations of high nickel, low copper surveillance RPV welds irradiated to high fluences,"** *J. Nuc. Mat*., 437 (2013) 107-115.

21. M.K. Miller, B.D. Wirth, and G.R. Odette, **"Precipitation in neutron-irradiated Fe-Cu and Fe-Cu-Mn alloys: a comparison of APT and SANS data,"** Materials Science and Engineering A533 (2003), pp. 133-139.

22. Nanstad, R. K., Miller. M. K., and Lewis, W. D., **"Results of Examinations of Surveillance Specimens from Commercial Reactors"** ORNL/TM-2012/447, Oak Ridge National Laboratory, September 2012.

INTERNAL DISTRIBUTION

Busby, J.T.	busbyjt@ornl.gov
Chen, X.	chenx@ornl.gov
Field, K. G.	fieldkg@ornl.gov
Ice, G.	icege@ornl.gov
Leonard, K.J.	leonardk@ornl.gov
Le Pape, Y. M.	lepapeym@ornl.gov
Littrell, K. C.	littrellkc@ornl.gov
Miller, M.K.	millermk@ornl.gov
Nanstad, R.K.	nanstadrk@ornl.gov
Naus, D.J.	nausdj@ornl.gov
Rosseel, T.M.	rosseeltm@ornl.gov
Snead, L. L.	sneadll@ornl.gov
Sokolov, M.A.	sokolovm@ornl.gov
Williams Jr, D.L.	williamsdljr@ornl.gov
Williams, G. T.	williamsgt@ornl.gov

EXTERNAL DISTRIBUTION

K. McCarthy, Idaho National Laboratory, P.O. Box 1625, Idaho Falls, ID 83415-3860, (Kathryn.Mccarthy@inl.gov)
R. Reister, GTN Bldg, 1000 Independence Ave, S.W. Washington, DC 20585, (Richard.Reister@nuclear.energy.gov)
P. Wells, Materials Department, University of California, Santa Barbara CA 93106-5050 (pwells@umail.ucsb.edu)
G. R. Odette, Department of Mechanical Engineering, 2343 Engineering II Building, University of California, Santa Barbara, CA 93106-5070 (Odette@engineering.ucsb.edu)
D. J. Sprouster, Brookhaven National Laboratory, Bldg 817, Upton, New York 11973 (dsprouster@bnl.gov)
L. E. Ecker, Brookhaven National Laboratory, Bldg 817, Upton, New York 11973 (lecker@bnl.gov)